A robust, dynamic R_2^*-and-field-map-corrected image reconstruction for single shot self-refocusing trajectories at 3T

Sangwoo Lee[1], Jeffrey A. Fessler[1], Douglas C. Noll[2]

[1]Department of Electrical Engineering and Computer Science,

University of Michigan, Ann Arbor, MI

[2]Department of Biomedical Engineering,

University of Michigan, Ann Arbor, MI

Full-paper draft submitted to the Journal of Magnetic Resonance in Medicine

February 23, 2006

Running head:	Robust, dynamic R_2^*-and-field-map corrected reconstruction
Manuscript word count:	5912 words
Correspondence to:	Sangwoo Lee
Address:	Functional MRI Laboratory, University of Michigan,
	2360 Bonisteel Ave, Ann Arbor,
	MI 48109-2108, USA.
Telephone number:	734-647-1996
Fax number:	734-938-4218
Email address:	sangwool@umich.edu
Grant sponsor:	NIH R01DA015410-01

1 ABSTRACT

The self-refocusing trajectories such as single shot rosette trajectory and projection reconstruction exhibit spectral selectivity, which makes the reconstruction very sensitive to off-resonance. In 3T MR, the off-resonance is often too high to reconstruct the images accurately using the existing field-map-corrected iterative reconstruction methods. Decomposing the k-space data into several small segments, we then apply spatio-temporally regularized iterative reconstruction, which uses prior knowledge on the temporal changes of the imaging object as additional information to reconstruct images. We propose a new R_2^*-and-field-map-corrected image reconstruction method and dynamic R_2^*-and-field-map estimation method. The simulation and functional experiment results show that the proposed methods provide robust reconstruction of the temporal evolution of the imaging object even with low accuracy initial field maps.

Key words: iterative image reconstruction, R_2^*, off-resonance, rosette, projection reconstruction

2 INTRODUCTION

Self-refocusing trajectories are defined as those k-space trajectories that sample the origin of k-space multiple times, forming multiple gradient echoes. Self-refocusing trajectories include multi-echo projection reconstruction (PR) trajectories [1, 2], and rosette trajectories [3, 4].

Multiple visits to the origin of the k-space cause the reconstructed images to be sensitive to off-resonance effects. This property is known as spectral selectivity in the literature on the rosette trajectories, and it is shared by other self-refocusing trajectories. Noll et al. used the spectral selectivity of rosette trajectories to selectively reconstruct different chemical species or multiple slices with different resonant frequencies [3, 4].

However, this property can create difficulties in image reconstruction for high field imaging. If the off-resonance frequency is high enough to move an image voxel out of the pass band of the spectral selectivity, the image intensity at the voxel will be significantly reduced. In this case, the artifact from field inhomogeneity is mainly local signal loss, rather than blurring in spiral imaging or geometric distortion in EPI (Echo Planar Imaging). The signal loss is exacerbated when single shot method is used, because the width of the pass band is inversely proportional to the acquisition length [3].

It is also known that R_2^* (or $1/T_2^*$) decay during the readout can cause streaking artifacts and blurring, if it is not accounted for in the reconstruction [2].

A standard approach to reduce the R_2^* and off-resonance artifact is to use fewer echo trains, or to use multi-shot methods. Conventionally, the acquisition time for an echo train is restricted to ensure relatively small magnitude and phase changes from R_2^* and off-resonance. However, this method can increase scan time, making it more susceptible to physiological noise and subject motion.

Another approach to reduce the artifact is to incorporate the off-resonance and/or R_2^* map in the reconstruction model [2, 3, 4, 5]. However, these methods depend on accurate pre-estimates of off-resonance and/or R_2^* maps. Due to the limited accuracy of the low resolution maps estimated from the same data, the acquisition length was still restricted to nine echoes [2], or the spatial resolution and field of view had to be reduced [3]. In addition, in high field imaging, it is often difficult to derive a field map for lower brain slices from single shot data, since the large off-resonance there leads to insufficient signal or significant distortion.

In this paper, we propose a spatio-temporally regularized iterative reconstruction method as a new approach to correct for the R_2^* and off-resonance artifacts in single shot self-refocusing trajectories. This method can accurately reconstruct R_2^*-and-field-map-corrected images for the single shot PR and rosette trajectories at 3T. It does not require a pre-determined R_2^* map, and only requires the initial guess of a low accuracy field map. Beyond the R_2^*-and-field-map-corrected reconstruction, the subimages generated by the method can be used in dynamic estimation of accurate R_2^* and field map by fitting the magnitude and phase time courses of each voxel to a complex exponential model.

Dynamic field mapping can improve image quality, for example, by capturing the fluctuation of the main field during functional imaging studies. Such fluctuations are caused by head movement, passive shim heating, and respiration [6]. The proposed method is suitable for addressing such fluctuations.

Dynamic R_2^* mapping has been used in a variety of MR applications [7, 8, 9, 10, 11, 12]. In functional MRI, dynamic R_2^* mapping provided nearly optimal functional contrast and activation volume [13], and better contrast to noise ratio than T_2^*-weighted imaging [8]. R_2^* is more closely linked to physiological parameters in functional MRI, which may allow for better inter-subject and inter-tissue comparisons, and the measurement can be more independent of scan parameters and hardware fluctuations.

Recently, there have been several studies that tried to estimate the field map and/or R_2^* map along with the proton density image, I_0, simultaneously from a single-shot gradient echo data, using trajectories such as spiral-in and out, multi-echo EPI, or rosette [6, 14, 15]. However, these methods were not able to address R_2^* decay [6], required high computational cost [14], or could detect only relatively small R_2^* changes between acquisitions via linearization [15]. Our proposed method estimates R_2^* decay and field map simultaneously without assuming small R_2^* changes.

In the following sections, we introduce a mathematical description of the proposed method, and a strategy to obtain the initial field map from single shot data. We also present an approach to determine the regularization parameters throughout simulations, as well as the functional imaging results. All simulations were conducted using both PR and rosette trajectories, while experiments were performed using single shot rosette trajectories.

3 THEORY

3.1 Self-refocusing trajectories and their R_2^* and off-resonance artifacts

The main difference between PR and rosette trajectory is the number of self-crossing points. The self-crossing point of PR is located only at the origin of k-space. In rosette trajectories, the number of self-crossing points can be controlled via the ratio between two frequencies ω_1 and ω_2, where the trajectories are described as [3]

$$\vec{k}(t) = \sin(\omega_1 t) e^{i\omega_2 t}. \tag{1}$$

Figure 1 shows examples of PR and rosette trajectories and corresponding pulse sequence diagrams.

If there is unwanted off resonance, the reconstructed images can lose intensity severely due to the spectral selectivity. In addition, R_2^* decay causes artifacts in the reconstruction unless it is properly addressed.

In the following section, we propose a spatio-temporally regularized iterative reconstruction method that can correct for the artifact from R_2^* and field map simultaneously.

3.2 Iterative image reconstruction with spatio-temporal regularization

The baseband signal $S(t)$ of MR with mono-exponential T_2^*(or $1/R_2^*$) decay can be modeled as [16]

$$S(t) = \int f_0(\vec{r}) e^{-R_2^*(\vec{r})t} e^{-i\omega(\vec{r})t} e^{-2\pi i \vec{k}(t)\cdot\vec{r}} d\vec{r}, \quad \tau_1 \leq t < \tau_{end}, \tag{2}$$

where $f_0(\vec{r})$ is the transverse magnetization at the beginning of the data acquisition; $R_2^*(\vec{r})$ is the R_2^* map in sec^{-1}; $\omega(\vec{r})$ is the B_0 field inhomogeneity; $\vec{r}$ is the spatial location vector; and τ_1 and τ_{end} are the beginning and the end of the acquisition respectively.

Assuming that the R_2^* decay is negligible during the lth time segment, $\tau_l \leq t < \tau_{l+1}$, we can rewrite (2) as

$$S_l(t) \approx \int f_l(\vec{r}) e^{-i\omega(\vec{r})t} e^{-2\pi i \vec{k}(t)\cdot\vec{r}} d\vec{r}, \quad \tau_l \leq t < \tau_{l+1}, \text{ and } l = 1, ..., L, \tag{3}$$

where L denotes the number of data segments, and $f_l(\vec{r}) = f_0(\vec{r}) e^{-R_2^*(\vec{r})TE_l}$ is the lth *subimage* with the echo time TE_l. We define TE_l as the beginning of each segment, $\mathrm{TE}_l = t_l$, and each segment has approximately equal size.

We discretize (3) in a matrix-vector form with additive complex white Gaussian noise $\epsilon \in \mathbb{C}^{M_l \times 1}$ as

$$\mathbf{Y}_l = \mathbf{A}_l \mathbf{X}_l + \epsilon, \tag{4}$$

where $\mathbf{Y}_l \in \mathbb{C}^{M_l \times 1}$ is the l'th segment of the measured complex MR signal; M_l denotes the number of data samples in the lth segment; $\mathbf{X}_l \in \mathbb{C}^{N \times 1}$ is the lth discrete subimage i.e., $[\mathbf{X}_l]_n = f_l(\vec{r}_n)$; and $\mathbf{A}_l \in \mathbb{C}^{M_l \times N}$ is the lth system matrix. The elements of $\mathbf{A}_l$ are

$$[\mathbf{A}_l]_{mn} = e^{-i2\pi\vec{k}(t_m)\cdot\vec{r}_n} e^{-i\hat{\omega}(\vec{r}_n)t_m}, \quad m = 1, ..., M_l \text{ and } n = 1, ..., N,$$

where $\hat{\omega}$ is an initial guess of the field map.

To ensure minimal signal change due to R_2^* decay, the length of each segment should be much smaller than T_2^*, i.e., a few miliseconds. If the individual subimages were directly reconstructed from each data segment, there would be artifacts from high levels of undersampling (Figure 2). To overcome the limited k-space coverage of each segment, additional information on the subimages is necessary.

In previous work, we used temporal evolution of the subimages based on the complex exponential model as the additional information to reduce the undersampling artifacts. The complex exponential model included the pre-estimated R_2^* map and the field map [17]. An extra penalty term penalized the subimages against the complex model, where the term was added to the cost function of iterative penalized least square reconstruction [18].

In this paper, we propose to penalize the second derivative of the time course of subimages. This temporal regularization is adequate to capture the temporal evolution of the magnitude and phase of the subimages. There are advantages to this temporal regularization scheme compared with our previous work. First, the new regularization scheme does not require the preestimation of R_2^* map. Second, it is more robust to the errors of the initial field map used in the reconstruction. Third, it is not limited to the mono-exponential model; instead it allows models with smoothly varying functions.

In the proposed regularization scheme, the penalty term is modified to regularize the second derivative of the temporal evolution of the subimages, which represent the object corresponding to each data segment. The final cost function ϕ consists of the data fit term, spatial regularization term for each subimage, and the temporal regularization term as

$$\phi \;=\; \sum_{l=1}^{L} \|\mathbf{Y}_l - \mathbf{A}_l(\hat{\omega})\mathbf{X}_l\|^2 + \beta \sum_{l=1}^{L} \|\mathbf{C}\mathbf{X}_l\|^2 + \gamma \sum_{l=2}^{L-1} \|\mathbf{X}_{l-1} - 2\mathbf{X}_l + \mathbf{X}_{l+1}\|^2, \tag{5}$$

where $\mathbf{C}$ is a spatially differencing matrix for the spatial smoothness penalty; β is the spatial resularization parameter; and γ is the temporal regularization parameter. The reconstruction of subimages is done by minimizing ϕ over the subimages $\mathbf{X}_l$'s as follows:

$$(\hat{\mathbf{X}}_1, \hat{\mathbf{X}}_2, ..., \hat{\mathbf{X}}_L) = \underset{\mathbf{X}_1, \mathbf{X}_2, ..., \mathbf{X}_L}{\operatorname{argmin}} \phi(\mathbf{X}_1, \mathbf{X}_2, ..., \mathbf{X}_L; \hat{\omega}). \tag{6}$$

In our experiment, we used the conjugate gradient iteration for minimization. Assuming that each time segment is sufficiently small, we model the reconstructed subimages $\hat{\mathbf{X}}_l$ as

$$[\hat{\mathbf{X}}_l]_n = f_l(\vec{r}_n) e^{-i(\omega(\vec{r}_n) - \hat{\omega}(\vec{r}_n))TE_l}. \tag{7}$$

From the magnitude of $\mathbf{X}_l$'s, we can estimate the R_2^* map by fitting to an exponential curve. If it is necessary, one can estimate the field map residual $\omega(\vec{r}) - \hat{\omega}(\vec{r})$ using a log-linear fit of the phase of subimages, and use the refined field map to re-estimate the subimages. However, the convergence of such an iteration is not guaranteed, and our preliminary simulation results show that there is only minimal improvement from reestimation with an updated field map. Figure 2 illustrates how the spatio-temporal regularized iterative reconstruction is done.

3.2.1 R_2^*-and-field-map-corrected reconstruction

Ideally, every subimage $\mathbf{X}_l$ reconstructed from the iterative scheme described in the previous section is R_2^* corrected, since the data segment size is small enough not to allow significant R_2^* decay in each of them. However, due to the structure of the temporal regularization and finite length of the acquired data, the first and last subimages have fewer neighbors to regularize with. This results in more artifacts in the subimages in near the boundary of data acquisition than the subimages in the middle of data acquisition.

Therefore, we simply choose the middle (L/2th) subimage among the subimages from the spatio-temporally regularized iterative reconstruction as the R_2^*-and-field-map-corrected image. The basic outlines of the procedure is described as dashed lines in Figure 2.

3.2.2 R_2^* and field map estimation from extended data set

The R_2^* map is estimated by least-square fitting the magnitude of the low-reconstruction-error subimages to a mono-exponential curve. Similarly, the field map is estimated from the sum of the initial field map and the log-linear fit of the phase of the subimages. In this procedure, we used the first half of the subimage sequence reconstructed from the spatio-temporally regularized iterative reconstruction.

Extending data acquisition results in more accurate R_2^* and field maps, since it has less proportion of subimages which are affected from the boundary effect. On the other hand, the length of acquisition is limited by hardware capability and the MR signal strength. Therefore, the length of extended data acquisition needs to be determined within those limitations. Figure 2 again illustrates the basic scheme of this procedure.

To get accurate estimates of $\mathbf{X}_l$'s, a few unknown terms in (6) must be predetermined. The following sections explain how to determine the initial field map and the design parameters.

3.3 The estimation of initial field map

Off resonance effects cause phase changes between the neighboring subimages. If the phase change is too large, the temporal regularization can reduce the difference in phase more than the difference in the magnitude. This causes artifacts in the subimages, and results in erroneous estimation of the R_2^* and field maps.

To avoid large phase changes, the *safe range* of the off-resonance can be defined as follows. Assuming that the time difference between neighboring subimages is about 4ms, the off-resonance cannot cause more than $\pi/4$ of phase difference during that period. Therefore the maximum allowable off-resonance will be 31Hz. We call this interval of off-resonance as the *operation range* of the temporal regularization for given length of data segment.

At 3T, the off-resonance frequency often exceeds 31Hz even with good shimming procedures. This is why the initial field map $\hat{\omega}$ is necessary in the proposed method. As is denoted in (7), the phase evolution of the estimated images depends on the difference between the unknown true field map and the initial field map. If the field map error is smaller, i.e. less than 31Hz, the spatio-temporally regularized reconstruction will result in less artifacts in the subimages.

On the other hand, for single-shot-self-refocusing trajectories at 3T, it is often difficult to achieve small error in the field map using the standard 'two-point' method [19]. The images with delayed echo time, which are to be used in estimating the field map, suffer severe image intensity loss due to the spectral selectivity. For example, a 25Hz of off-resonance will cause significant loss of image intensity for 40ms-long single-shot rosette acquisition, since the FWHM (Full Width Half Maximum) of spectral selectivity is the inverse of acquisition length [4].

To estimate the initial field maps with errors within the *operation range* of the temporal regularization for single-shot-self-refocusing trajectories at 3T, we improved the 'two-point' method to ignore incoherent data points in the reconstruction of images with different echo times. We choose a grid in an area near the center of k-space, reconstruct low resolution images at different echo time using only first data point that visits each grid point. Using this method, from a pair of rosette data with echo time difference of 2.5ms, we estimated a field map with the RMSE (Root Mean Squared Error) 6.79Hz, where the maximum absolute off-resonance of the true field map was 80.4Hz. Figure 3 compares the field maps from the standard 'two-point' method and our improved method.

3.4 Determining the design parameters

Spatial regularization is known to introduce a trade off between spatial smoothness and image noise variance [20]. High βs would result in the loss of the spatial resolution of the subimages $\mathbf{X}_l$s and the estimated R_2^* map, while low βs would cause unwanted amplification of the noise. The temporal regularization parameter γ has similar effect in the temporal direction. Excessive temporal regularization would cause the time course of subimages resemble a straight line, introducing bias in the R_2^* estimates with less variance. On the other hand, low temporal regulraization would bring in more undersampling artifact in the subimages, which will introduce noisy time course of subimages.

The number of segments L and the total data length play an important role in the accuracy and the speed of the reconstruction. For a given length of data, one could choose very large L to reduce the approximation error of R_2^* decay during each data segment. However, smaller data segments will introduce more undersampling artifact despite temporal regularization, and require more memory and computation time.

Choosing the right set of design parameters is another challenging task. In this paper, we determined the design parameters given a data set in simulations and experiments. Section 4 describes how this was done.

4 SIMULATIONS

4.1 Method

The simulations were conducted using 64×64 discrete image, R_2^* map and field map as shown in Figure 4. The k-space data was generated using direct implementation of equation (4) without noise. We implemented the reconstruction based on the NUFFT (NonUniform Fast Fourier Transform) representation of the MR system matrix [1][21] in MATLAB (Mathworks Inc. Natick, MA). 300 iterations were used for all simulations.

The PR and rosette trajectories shown in Figure 1 were used with variations in the number of extra spokes or petals. PR trajectories had 128 spokes for the estimation of the R_2^* and field maps, and 64 spokes for R_2^*-and-field-map corrected reconstruction. Each spoke had 128 samples, and the sampling time was 4μs. For simplicity, no transition time between the spokes was assumed for simplicity.

Rosette trajectories had the fast radial frequency $\omega_1/2\pi$=1.087 kHz, and slow angular frequency $\omega_2/2\pi$=113.22Hz. For R_2^*-and-field-map corrected reconstruction, these choices led to 48 cycles of radial oscillation, and for R_2^*-and-field-map estimation, the extended trajectory had 96 cycles of radial oscillation. The readout lengths of the rosette trajectories were 44.4ms and 88ms respectively with sampling time of 4μs. The time segmentation of trajectory was done carefully so that each segment had almost the same number of spokes or petals. For rosette trajectories, each segment started from the center of the k-space.

4.2 Determining the design parameters

The design parameters were determined by simulations. Using the synthesized k-space data, the subimages were reconstructed with a range of β, γ, and L values. For these simulations only, the reference field map was used as the initial field map, since this choice should provide the best achievable reconstruction performance. For each reconstruction, the NRMSEs (Normalized Root Mean Squared Error) of the magnitude subimages with respect to the R_2^*-weighted reference images were measured, and the minimum values of the NRMSEs were compared for various values of the design parameters.

Figure 5 shows the minimum NRMSEs for the various values of β, γ, L and acquisition length. The β and γ values that gave the minimum reconstruction error depended on the length of segment rather than the acquisition length or L. In addition, the overall NRMSE was lowest when each segment included two spokes or petals.

From the simulations, the best spatial regularization parameter β was chosen as 1, the temporal regularization parameter γ was 400, and the number of data segments L was 32 for the PR trajectory of 64 spokes.

We also performed similar simulations for the rosette trajectories (not shown).

4.3 R_2^*-and-field-map-corrected image reconstruction

For comparison, we performed four different simulations. First, we reconstructed the field-map-corrected T_2^*-weighted image using fast iterative reconstruction [21]. In this method, we used the reference field map in the reconstruction system model to highlight the artifact from R_2^* decay during the data acquisition (Figure 6 (a)). Second, instead of the reference field map, we used the initial field map estimated from the method described in section 3.3. The standard fast iterative reconstruction reveals that the estimation error of the initial field map causes significant amount of artifacts in the reconstructed image (Figure 6 (b)). Third, the initial field map was also used in the proposed R_2^*-and-field-map-corrected reconstruction (Figure 6 (c)), and the reference field map was again used in the proposed R_2^*-and-field-map-corrected reconstruction method (Figure 6 (d)). The design parameters determined in the previous section were used in the reconstructions. Figure 6 (c) and (d) indicate that the proposed R_2^*-and-field-map-corrected reconstruction method not only reduces most of the artifacts from both R_2^* decay and field map error but is also robust to the error in the initial field map. Note that the most of the remaining artifact in the proposed method (Figure 6 (c)) is local to the area where the error in the initial field map was highest (47.9 Hz) in the region of interest.

For rosette trajectories, we achieved similar results, where the NRMSE of no R_2^*-corrected image was 0.376, NRMSE of the field-corrected image using the initial field map was 0.369, and the NRMSE of the proposed method using the initial field map was 0.047.

4.4 R_2^*-and-field-map estimation

Using the design parameters determined from section 4.2 (β=1, γ=400, L=64, PR trajectory with 128 spokes), we estimated the R_2^* and field maps using the proposed method (Figure 7). The area where higher error in the initial field map presents showed more error in the estimated R_2^* map. The accuracy of the field map was significantly improved by the proposed R_2^*-and-field-map estimation method over using only the initial field map.

While the extended acquisition length increased the accuracy of the reconstructed subimages, it also increased the sensitivity of R_2^* map estimation to the error of the initial field map. Table 1 shows the result of the simulations for various values of the reference and the initial field maps. The proposed method improved the accuracy of the field maps from the initial field maps, but the accuracies of the estimated R_2^* maps were affected at the locations where the errors in the initial field maps were high.

5 EXPERIMENTAL STUDY

5.1 Method

All MRI data were acquired on a 3T scanner (GE Signa, Milwaukee, WI). Written informal consent was obtained from subjects prior to the MRI scan. Two MRI experiments were performed on human subjects.

Experiment I : For the R_2^*-and-field-map-corrected image reconstruction, five measurements were acquired for twenty contiguous slices with 3mm thickness. The scan parameters were TR = 2s, TE = 5ms, and FOV = 20cm, where TE was defined as the beginning of the rosette acquisition. The first time point was delayed by 2.5ms to estimate the initial field map as described in section 3.3. The parameters for the rosette trajectory were kept the same as in the section 4. Total readout was 44.4ms. Each session was preceded by non slice selective fat presaturation pulse. The R_2^*-and-field-map-corrected reconstruction was done based on the design parameters determined from simulations (β=1, γ=150, L=24).

Experiment II : For the R_2^*-and-field-map estimation, ten contiguous slices (slice thickness = 3mm) were acquired while a functional imaging study was conducted. An 8Hz flickering checker board was used as visual stimulation to the subject, while finger tapping task was asked to be performed during the visual stimulus. The visual stimulus was presented for 5 cycles with 20s off/20s on. The scan parameters were kept the same as those used in the first experiment, and the initial field map was also estimated from the delayed acquisitions. The readout was 88ms for the extended rosette acquisition.

Four different volumes of time series were reconstructed from the functional study data acquired in experiment II.

1. The first volume of dynamic R_2^* maps was reconstructed applying the proposed R_2^*-and-field-map estimation method to the entire 88ms acquisition data (β=1, γ=150, L=48).

2. The second volume was chosen as the time series of the 24th subimage among the subimages, which were already reconstructed using the proposed spatio-temporally regularized iterative reconstruction for the first volume.

3. The third volume was the time series of the static field-map-corrected T_2^*-weighted images

using the fast iterative reconstruction [21]. At each time point, the image was reconstructed using the static field map estimated from the proposed R_2^*-and-field-map estimation method at the first time point. The reconstruction was done on the middle segment of the extended data, which started at 20ms from the beginning of the acquisition and ended at 62ms of the acquisition to match the effective echo time of the 24th subimage.

4. The fourth volume was the time series of the dynamic field-map-corrected T_2^*-weighted images using the fast iterative reconstruction. At each time point, the image was reconstructed using the dynamic field map estimated from the proposed R_2^*-and-field-map estimation method. The reconstruction was done on the same segment of the data as the third volume.

The NRMSE of the current iteration with respect to the previous iteration was used as the stopping criterion for the conjugate gradient iteration in the proposed methods. We stopped the iteration when the NRMSE of current iterate gets smaller than 10^{-4}. About 460 iterations were needed to reach that error level for the R_2^*-and-field-map estimation method. The number of iterations varied widely according to the choice of design parameters and the acquisition lengths.

5.2 Results

Figure 8 and figure 9 show the image reconstruction results from the first MRI experiment (Experiment I). Figure 8 shows all of the 24 subimages reconstructed using the proposed R_2^*-and-field-map-corrected reconstruction method. As was found in the simulation results, the later echo subimages had more artifact than those in the middle. The streaking artifact present in the earlier echo subimages are due to imperfect fat presaturation, and to error in the initial field map. The subimages clearly show the temporal evolution of the R_2^* contrast between brain tissues and CSF in ventricles.

Figure 9 compares the standard field-map-corrected/uncorrected T_2^*-weighted image with that of the proposed R_2^*-and-field-map-corrected reconstruction method. The image from the proposed R_2^*-and-field-map-corrected reconstruction successfully recovered the signal in the high off-resonance area, where the image without field map correction lost most of the intensity (Figure 9 (a) and (c)). Figure 9 (b) shows the field-map-corrected T_2^*-weighted image with the initial field map estimated using the improved 'two-point' method in section 3.3.

The following figures show the results from the second functional MRI experiment (Experiment II). Figure 10 shows the R_2^* and field map of the 10th time point of the 7th slice estimated from the proposed R_2^*-and-field-map estimation method. The R_2^* map exhibits the anatomical structure of the brain, and the high field map area (bottom of the R_2^* map) shows no artifact from the field map error.

Figure 11 shows the results of four different reconstructions on the functional study data. The first row shows the activation map and the averaged time course of the dynamic R_2^* maps estimated using the proposed R_2^*-and-field-map-estimation method. The second row shows the activation map from the 24th subimages reconstructed using the proposed spatio-temporally iterative reconstruction method. The third and fourth row show the results from the static and dynamic field-map-corrected T_2^*-weighted images using fast iterative reconstruction [21]. For each reconstruction, the numbers of the activated pixels were 16, 18, 20 and 23 pixels repectively.

Figure 12 (a) shows the normalized averaged time series of one slice in the functional study. We regressed out the reference waveform using linear least square fitting before averaging the time series over the entire brain region. Only the time series of static field-map-corrected T_2^*-weighted image exhibits the time varying trend of the field map during the functional study. Figure 12 (b) shows the average time course of the dynamic field map estimated using the proposed R_2^*-and-field-map-estimation method.

6 DISCUSSION

Most of the error in the R_2^* estimates came from mismatch between the point spread functions (PSF) of subimages. We observed that the earlier images had enhancement in the edges of the simulation object, and the later subimages had smoother edges as shown in Figure 7. The error in the field map estimates was also concentrated around the edge of the simulation object. This result is the opposite to the results observed in [22], which used multi-spin echo radial data, and it is an interesting research problem to consider the effect of the spatio-temporal sampling scheme on the PSF of images. Preliminary data shows that this PSF mismatch could be reduced with well designed temporally varying γ values, and further investigation is required. Separate spatial regularization of the magnitude and phase of subimages [23] may also help to reduce the artifact.

Since there is no mono-exponential decay assumed in the reconstruction model, the subimages can also exhibit multi-exponential decays. Other preliminary results (not shown) indicate that the proposed scheme can reconstruct bi-exponential decays in the subimages. However, a robust nonlinear estimation algorithm is required to estimate the amplitudes and decay values from a single decay curve.

In this paper, the parameters for the PR and rosette trajectories were not optimized. A random view ordering of PR provided less error in the R_2^* estimates than the sequential order. This can be explained by considering the sampling in 3D k-t space. The randomized view ordering provides more evenly distributed sampling in 3D than sequential ordering, therefore it allows better condition for the reconstruction scheme to estimate the missing points in the k-t space. However, randomized view ordering would require more scan time due to the increased transition time between spokes. The rosette trajectory can provide a pseudo-randomized view ordering without increased transition time between petals.

The proposed method can be easily extended to multi-shot methods and the partially parallel imaging methods [24, 25] to speed up the acquisition or to improve the accuracy of estimates. In addition, dynamic imaging methods such as UNFOLD [26] use a series of undersampled trajectories to collect the data and applies a temporal low-pass filter to reduce the aliasing artifacts on each frame. The proposed method can be easily extended to reconstruct the unaliased images without specific temporal filters.

In the functional study, it was observed that the number of activated pixels was the smallest in the R_2^* mapping. One of the reasons could be the erroneous estimate of R_2^* maps due to the artifacts from the residual fat signal and the field map errors as shown in Figure 8. On the other side, the dynamic field-map-corrected images generated more activated pixels than the static field-map-corrected images in accordance with the results in [6].

The proposed R_2^*-and-field-map reconstruction method successfully reconstructed the R_2^*-and-field-map corrected image in the simulations. This indicates that the proposed method is robust to the R_2^*-and-field-map errors in the system model. The maximum allowable field map error can be calculated using the length of data segment as described in section 3.3. In addition, given the initial field map within the maximum allowable range of field map error, the proposed R_2^*-and-field-map estimation method was able to provide not only the dynamic field maps but also dynamic field-map-corrected subimages. The method requires an initial guess of the static (or dynamic if possible) field map, but it is obvious that the method is able to produce dynamic information of the field map change as it was presented in the functional study results.

The biggest concern of the proposed method is the reconstruction speed. A new faster iterative reconstruction method such as [27] could help to reduce the reconstruction time significantly. A well designed preconditioner [28] and good initial guess of subimages will also help to reduce the reconstruction time.

7 CONCLUSION

We have proposed a spatio-temporally regularized iterative reconstruction method to reconstruct R_2^*-and-field-map-corrected images and to estimate dynamic R_2^* and field maps. The proposed method required no *a priori* knowledge of R_2^* map, but only pre-estimated low accuracy field map was required. Through simulations and functinoal experiments, we verified that the method is capable of the accurately reconstructing the R_2^*-and-field-map-corrected images and estimating the dynamic R_2^* and field maps.

References

[1] V. Rasche, D. Holz, and R. Proksa. MR fluoroscopy using projection reconstruction multi-gradient-echo (prMGE) MRI. *Magnetic Resonance in Medicine*, 42:324–334, 1999.

[2] H. Eggers and P. Boesiger. Iterative ΔB_0 and T_2^* correction for radial multi-gradient-echo imaging. In *ISMRM Tenth Scientific Meeting*, page 348, 2004.

[3] D. C. Noll, S. J. Peltier, and F. E. Boada. Simultaneous multislice acquisition using rosette trajectories (SMART): A new imaging method for functional MRI. *Magnetic Resonance in Medicine*, 39:709–716, 1998.

[4] D. C. Noll, S. J. Peltier, and F. E. Boada. Multishot rosette trajectories for spectrally selective MR imaging. *IEEE Transactions on Medical Imaging*, 16:372–377, 1997.

[5] H. Eggers, T. Schaeffter, B. Aldefeld, and P. Boesiger. Combined δ B_0 and t_2^* correction for radial multi-gradient-echo imaging. In *ISMRM Ninth Scientific Meeting*, page 478, 2003.

[6] B.P. Sutton, D.C. Noll, and J.A. Fessler. Dynamic field map estimation using a spiral-in/spiral-out acquisition. *Magnetic Resonance in Medicine*, 51:1194–1204, 2004.

[7] S. Clare, S. Francis, P. G. Morris, and R. Bowtell. Single-shot T2* measurement to establish optimum echo time for fmri: Studies of the visual, motor, and auditory cortices at 3.0T. *Magnetic Resonance in Medicine*, 45:930–933, 2001.

[8] S. Posse, S. Wiese, D. Gembris, K. Mathiak, C. Kessler, M.-L. Grosse-Ruyken, B. Elghahwagi, T. Richards, S. R. Dager, and V. G. Kiselev. Enhancement of BOLD-contrast sensitivity by single-shot multi-echo functional MR imaging. *Magnetic Resonance in Medicine*, 42:87–97, 1999.

[9] M. Barth, J.R. Reichenbach, R.Venkatesan, E. Moser, and E.M. Haacke. High-resolution, multiple gradient-echo functioal MRI at 1.5T. *Magnetic Resonance Imaging*, 17:321–329, 1999.

[10] G. H. Glover, S. K. Lemieux, M. Drangova, and J. M. Pauly. Decomposition of inflow and blood oxygen level-dependent (BOLD) effects with dual-echo spiral gradient-recalled echo (GRE) fMRI. *Magnetic Resonance in Medicine*, 35:299–308, 1996.

[11] O. Speck and J. Hennig. Functional imaging by I0- and T2*-parameter mapping using multi-image EPI. *Magnetic Resonance in Medicine*, 40:243–248, 1998.

[12] C. Schwarzbauer and W. Heinke. Investigating the dependence of bold contrast on oxidative metabolism. *Magnetic Resonance in Medicine*, "41":"537–543", "1999".

[13] A. B. Wennerberg, T. Jonsson, H. Forssberg, and T. Li. A comparative fmri study: T2*-weighted imaging versus R2* mapping. *NMR in Biomedicine*, 14:41–47, 2001.

[14] D.B. Twieg. Parsing local signal evolution directly from a single-shot MRI signal: A new approach for fMRI. *Magnetic Resonance in Medicine*, 50:1043–1052, 2003.

[15] V.T. Olafsson, D.C. Noll, and J.A. Fessler. New approach for estimating dR2* in fMRI. In *ISMRM Ninth Scientific Meeting*, page 132, 2003.

[16] D. G. Nishimura. Principles of magnetic resonance imaging. Department of Electrical Engineering: Stanford University, 1996.

[17] Lee S., Noll D.C., and Fessler J.A. EXTended Rosette ACquisition technique (EXTRACT): A dynamic R2* mapping method using extended rosette trajectory. In *ISMRM Tenth Scientific Meeting*, page 2128, 2004.

[18] J. A. Fessler. Penalized weighted least-squares image reconstruction for positron emission tomography. *IEEE Transactions on Medical Imaging*, 13(2):290–300, 1994.

[19] E. Schneider and G. Glover. Rapid in vivo proton shimming. *Magnetic Resonance in Medicine*, 18:335–347, 1991.

[20] J. A. Fessler and W. L. Rogers. Spatial resolution properties of penalized-likelihood image reconstruction: space-invariant tomoraphs. *IEEE Transactions on Image Processing*, 5:1346–1358, 1996.

[21] B. Sutton, D. Noll, and J. Fessler. Fast, iterative image reconstruction for MRI in the presence of field inhomogeneities. *IEEE Transactions on Medical Imaging*, 22:178–188, feb 2003.

[22] M.I. Altbach, A. Bilgin, Z. Li, E.W. Clarkson, and T.P. Trouard. Processing of radial fast spin-echo data for obtaining t_2 estimates from a single k-space data set. *Magnetic Resonance in Medicine*, 54:549–559, 2005.

[23] J.A. Fessler and D.C. Noll. Iterative image reconstruction in MRI with separate magnitude and phase regularization. In *Proc. IEEE International Symposium on Biomedical Imaing*, page 209, 2004.

[24] D. K. Sodickson and W. J. Manning. Simultaneous acquisition of spatial harmonics (SMASH): fast imaging with radiofrequency coil arrays. *Magnetic Resonance in Medicine*, 38:591–603, 1997.

[25] K.P. Pruessmann, M. Weiger, M. B. Scheidegger, and P. Boesiger. SENSE: Sensitivity encoding for fast MRI. *Magnetic Resonance in Medicine*, 42:952–962, 1999.

[26] B. Madore, G. H. Glover, and N. J. Pelc. Unaliasing by fourier-encoding the overlaps using the temporal dimension (UNFOLD), applied to cardiac imaging and fMRI. *Magnetic Resonance in Medicine*, 42:813–828, 1999.

[27] J.A. Fessler, S. Lee, V.T. Olafsson, H.R. Shi, and D.C. Noll. Toeplitz-based iterative image reconstruction for MRI with correction for magnetic field inhomogeneity. *IEEE Transactions on Signal Processing*, 53:3393–3402, 2005.

[28] L. N. Trefethen and III D. Bau. *Numerical Linear Algebra*. SIAM, 1997.

LIST OF SYMBOLS

1. R_2^* : 2D R_2^* decay map
2. $\vec{k}(t)$: k-space trajectory
3. ω_1 : radial frequency of rosette trajectory
4. ω_2 : angular frequency of rosette trajectory
5. $S(t)$: MR baseband signal
6. $\vec{r}$: 2D spatial location vector
7. f_0 : transverse magnetization at the beginning of the data acquisition
8. $\omega(\vec{r})$: B_0 field inhomogeneity
9. τ_1 : beginning of the acquisition
10. τ_end : end of the acquisition
11. t : time
12. $S_l(t)$: baseband signal for lth segment
13. $f_l(\vec{r})$: transverse magnetization of lth segment
14. L : number of the segments
15. τ_l : beginning of the lth segment
16. TE_l : echo time of lth segment
17. ϵ : a M_l by 1 noise vector
18. M_l : number of data sample of lth segment
19. $\mathbf{Y}_l$: measured data samples of lth segment
20. $\mathbf{A}_l$: system matrix of lth segment
21. $\mathbf{X}_l$: lth discrete subimage
22. N : number of discrete voxels in FOV

23. $\hat{\omega}$: initial guess field map

24. T_2^* : $1/R_2^*$

25. ϕ : cost function

26. β : spatial regularization parameter

27. $\mathbf{C}$: spatially differencing matrix

28. γ : temporal regularization parameter

29. $\mathbf{X}_l$: estimated lth subimage

Notes

[1]The free software can be found in http://www.eecs.umich.edu/˜fessler

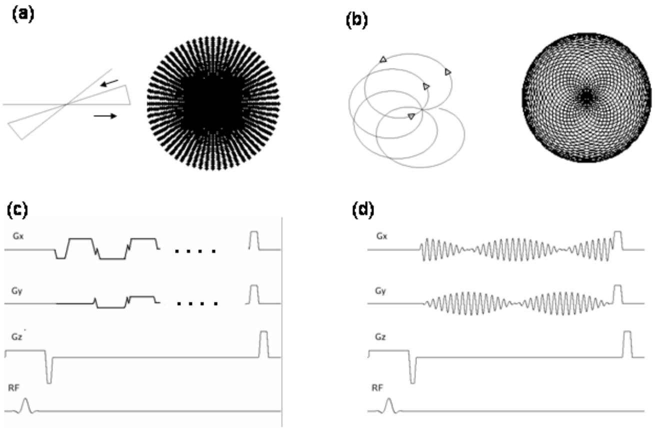

Figure 1: (a) Single shot PR trajectory (sequential view ordering) (b) single shot rosette trajectory (c) single shot PR pulse sequence (d) single shot rosette sequence

FIGURES AND TABLES

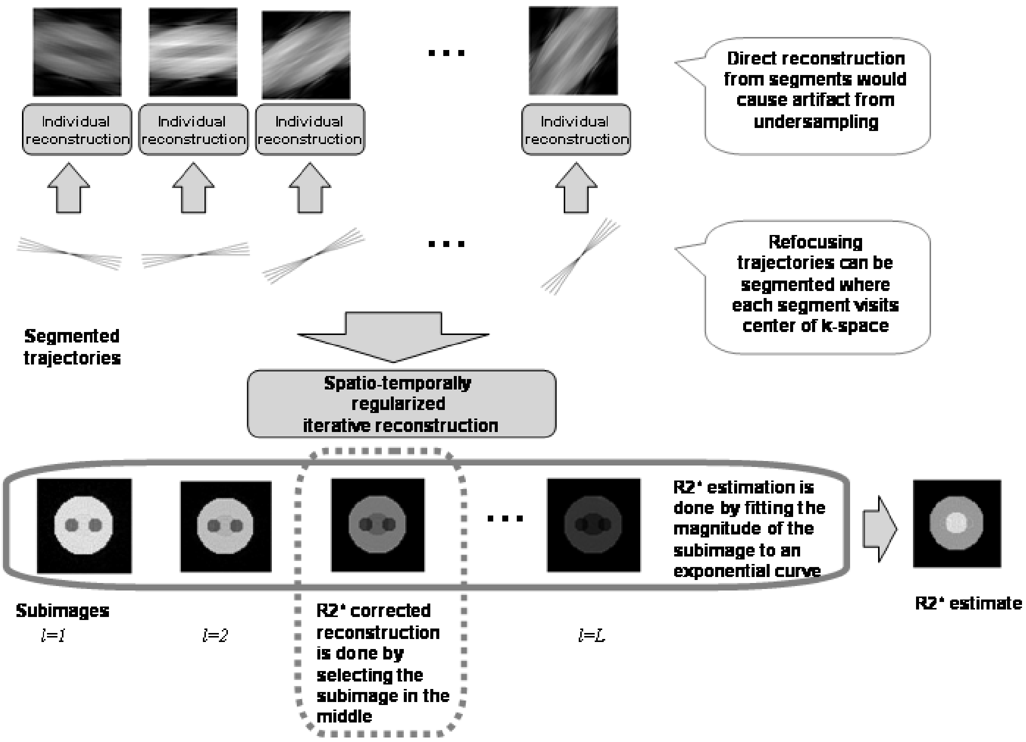

Figure 2: The proposed R2* corrected reconstruction scheme (dotted line) and dynamic R2* estimation (solid line)

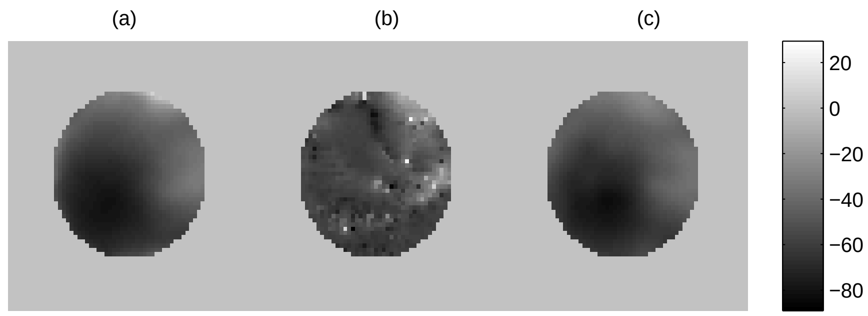

Figure 3: (a) The reference field map. (b) Estimated field map from conventional 'two-point' method (RMSE = 14.23Hz, Max error = 98.5Hz). (c) Estimated field map from the proposed field map estimation method (RMSE = 3.43Hz, Max error = 34.46Hz).

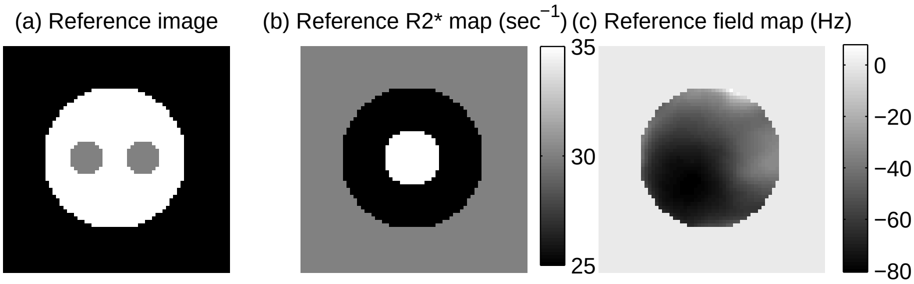

Figure 4: The reference image (a), R_2^* map (b), and field map (c) used in simulations

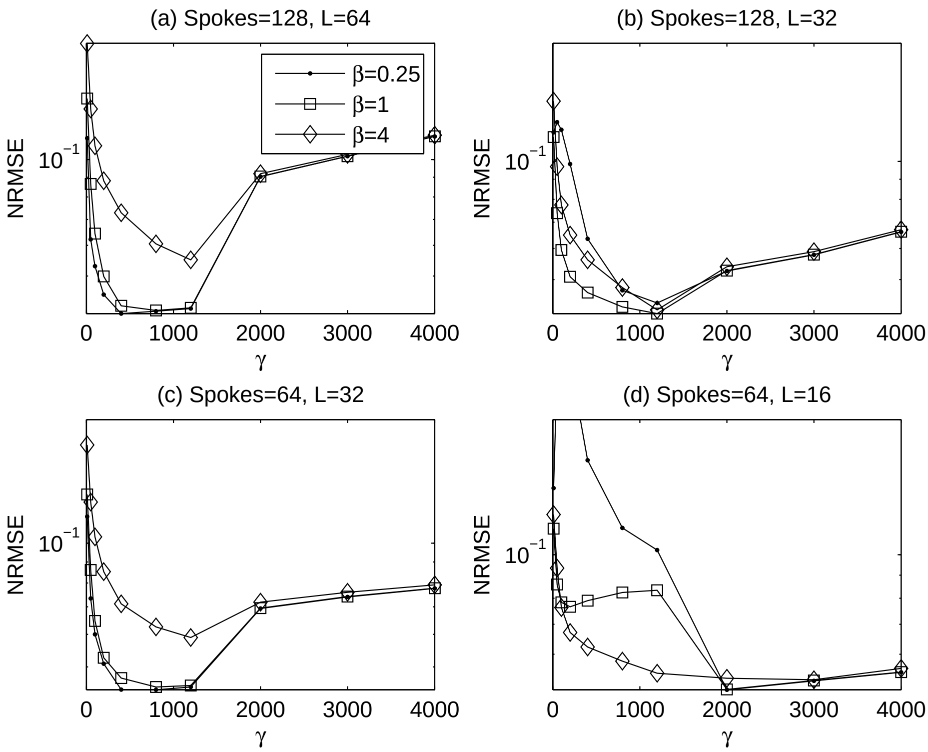

Figure 5: The minimum NRMSE of subimages with different β and γ values for various data lengths and numbers of segments.

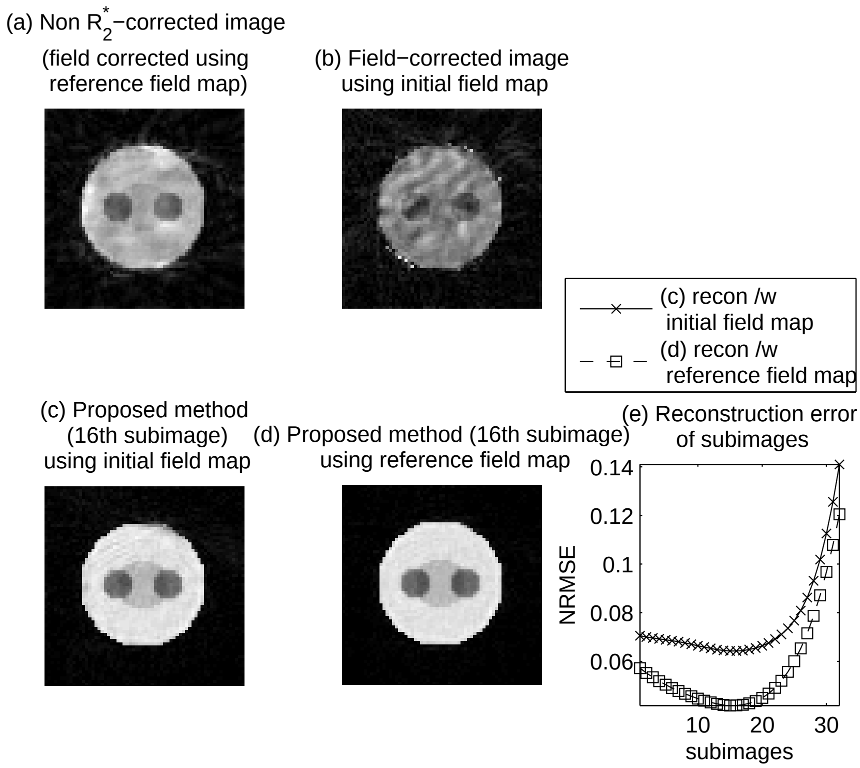

Figure 6: (a) Field-map-corrected image using the reference field map without R_2^* correction (NRMSE=0.28), (b) field-map-corrected T_2^*-weighted image using the initial field map without R_2^* correction (NRMSE=0.31), (c) proposed method with the initial field map (16th subimage, NRMSE=0.064), (d) proposed method with the reference field map (16th subimage, NRMSE=0.042). (e) The NRMSE of each subimage for (c) and (d). The maximum error in the initial field map was 47.9Hz with RMSE of 3.1Hz. The design parameters for the proposed method were β=1, γ=400, L=32.

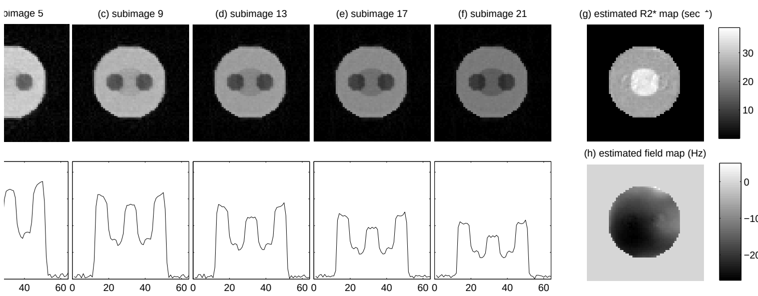

Figure 7: (a) (f) The subimages (l=1,5,9,13,17,21) and their profiles. (g) the estimated R_2^* map (RMSE $= 1.32sec^{-1}$) and (h) the estimated field map (RMSE = 0.52Hz).

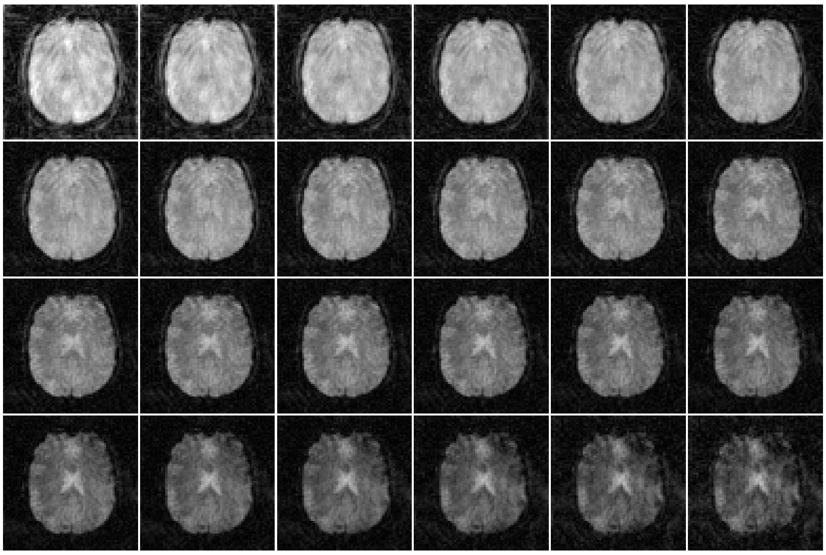

Figure 8: Experiment I : The 24 reconstructed subimages from a single shot gradient echo rosette data set (readout = 44.4ms). The left top image is the first subimage.

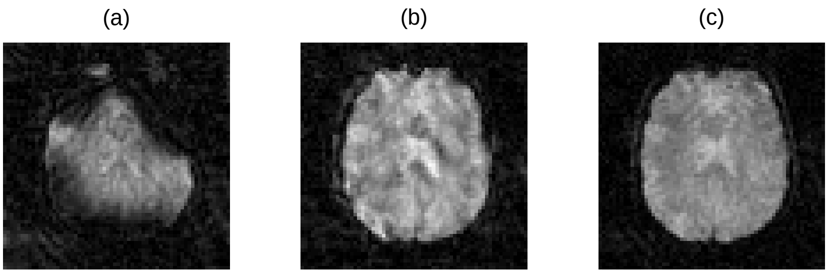

Figure 9: Experiment I : (a) Image without field map correction. (b) Field-map-corrected T_2^*-weighted image reconstructed from standard iterative reconstruction. (c) Proposed R_2^*-and-field-map-corrected reconstruction (12th subimage in Figure 8). In (b) and (c), the initial field map, which was estimated using the method described in section 3.3, was used in the reconstructions.

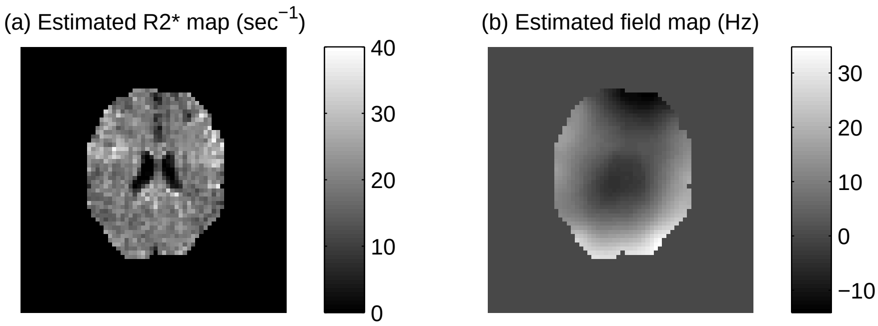

Figure 10: Experiment II : The estimated R_2^* map and field map from the proposed R_2^*-and-field-map estimation method.

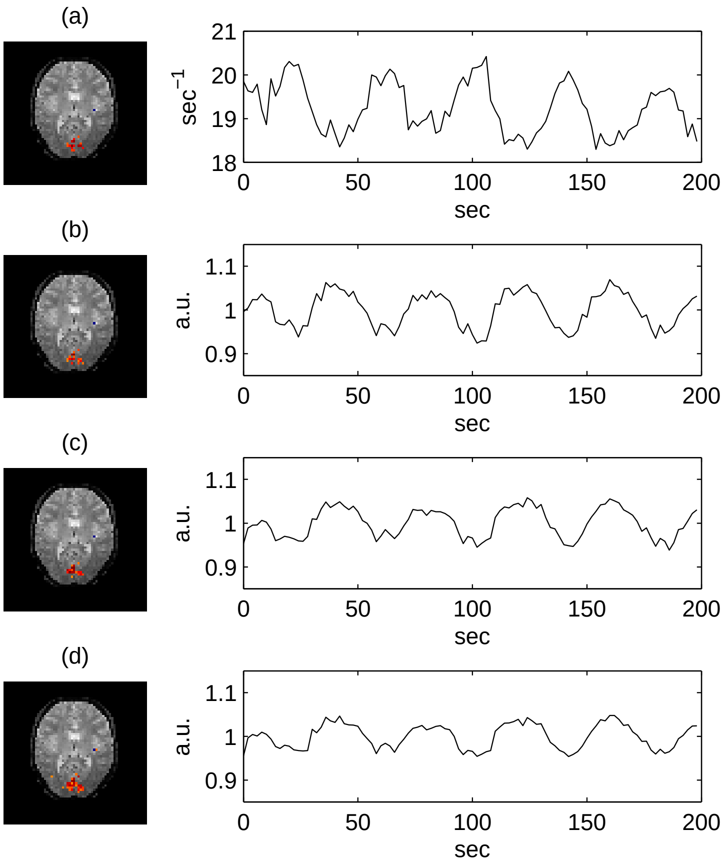

Figure 11: Experiment II : Activation maps (left) and the corresponding averaged time course of the activated pixels (right). (a) The dynamic R_2^* maps from the proposed R_2^*-and-field-map-estimation method. (b) The 24th subimages from the proposed R_2^*-and-field-map-estimation method. (c) The field-map-corrected T_2^*-weighted images with static field map estimated from the first time point. (d) The dynamic field-map-corrected T_2^*-weighted images, where dynamic field maps were estimated from the proposed R_2^*-and-field-map-estimation method.

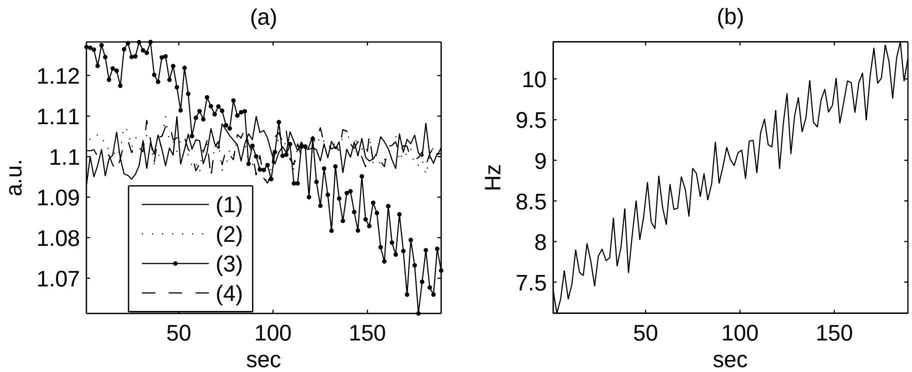

Figure 12: Experiment II : (a) The normalized mean time series of the four experiments from Fig. 11. Each line represents the time series of the R_2^* maps from the proposed R_2^*-and-field-map estimation method (1), the 24th subimages from the proposed R_2^*-and-field-map estimation method (2), the field-map-corrected T_2^*-weighted images using the field map estimated from the first time point (3), and the dynamic field-map-corrected T_2^*-weighted images using the field maps estimated from the proposed R_2^*-and-field-map-estimation method (4). (b) The average time course of the dynamic field map estimated using the proposed R_2^*-and-field-map-estimation method.

	Initial field map		Estimated field map		Estimated R_2^* map	
	RMSE	max.error	RMSE	max.error	RMSE	max.error
Field map 1	0.86 Hz	8.02 Hz	0.52 Hz	2.99 Hz	1.32 s^{-1}	7.77 s^{-1}
Field map 2	2.27 Hz	20.50 Hz	0.68 Hz	4.34 Hz	1.97 s^{-1}	16.03 s^{-1}
Field map 3	3.27 Hz	31.71 Hz	0.91 Hz	8.73 Hz	3.11 s^{-1}	24.87 s^{-1}

Table 1: Estimation errors of the field maps and R_2^* maps for synthesized data sets with different field map magnitudes. Field map 3 (max amplitude = 79.1 Hz) is identical to the reference field map shown in Fig. 4. Field maps 1 (max amplitude = 26.4 Hz) and 2 (max amplitude = 52.7 Hz) are obtained by scaling field map 3 by 0.33 and 0.67, repectively.